Bayesian implications of current LHC and XENON100 search limits for the CMSSM

Andrew Fowlie,[1,*] Artur Kalinowski,[2,†] Malgorzata Kazana,[3,‡] Leszek Roszkowski,[3,§,¶] and Y.-L. Sming Tsai[3,‖]

(BayesFITS Group)

[1]*Department of Physics and Astronomy, University of Sheffield, Sheffield S3 7RH, United Kingdom*
[2]*Department of Physics, University of Warsaw, Hoża 69, 00-681 Warsaw, Poland*
[3]*National Centre for Nuclear Research, Hoża 69, 00-681 Warsaw, Poland*
(Received 2 December 2011; published 12 April 2012)

The CMS Collaboration has released the results of its search for supersymmetry, by applying an α_T method to 1.1/fb of data at 7 TeV. The null result excludes (at 95% C.L.) a low-mass region of the Constrained MSSM's parameter space that was previously favored by other experiments. Additionally, the negative result of the XENON100 dark matter search has excluded (at 90% C.L.) values of the spin-independent scattering cross sections $\sigma_p^{\rm SI}$ as low as 10^{-8} pb. We incorporate these improved experimental constraints into a global Bayesian fit of the Constrained MSSM by constructing approximate likelihood functions. In the case of the α_T limit, we simulate detector efficiency for the CMS α_T1.1/fb analysis and validate our method against the official 95% C.L. contour. We identify the 68% and 95% credible posterior regions of the CMSSM parameters, and also find the best-fit point. We find that the credible regions change considerably once a likelihood from α_T is included, in particular, the narrow light Higgs resonance region becomes excluded, but the focus point/horizontal branch region remains allowed at the 1σ level. Adding the limit from XENON100 has a weaker additional effect, in part due to large uncertainties in evaluating $\sigma_p^{\rm SI}$, which we include in a conservative way, although we find that it reduces the posterior probability of the focus point region to the 2σ level. The new regions of high posterior favor squarks lighter than the gluino and all but one Higgs bosons heavy. The dark matter neutralino mass is found in the range 250 GeV $\lesssim m_\chi \lesssim$ 343 GeV (at 1σ) while, as the result of improved limits from the LHC, the favored range of $\sigma_p^{\rm SI}$ is pushed down to values below 10^{-9} pb. We highlight tension between $\delta(g-2)_\mu^{\rm SUSY}$ and $\mathcal{BR}(\bar{B}\to X_s\gamma)$, which is exacerbated by including the α_T limit; each constraint favors a different region of the CMSSM's mass parameters.

DOI: 10.1103/PhysRevD.85.075012 PACS numbers: 12.60.Jv, 12.10.Dm, 12.10.Kt

I. INTRODUCTION

The search for new physics at the Large Hadron Collider (LHC) began in earnest last year. An initial data set of about 35/pb at $\sqrt{s}=7$ TeV was followed this year by a much larger collection of about 5/fb of data. Based on about 1/fb of analyzed data, earlier this year new limits were published by ATLAS [1] and CMS [2] experimental collaborations which significantly improved early LEP [3] and recent Tevatron results [4] as well as their own initial exclusion limits on the mass scale of low-energy supersymmetry (SUSY), in particular, on the mass parameter space of the Constrained MSSM (CMSSM) [5].

The CMSSM is a tractable unified model of effective softly broken supersymmetry, which includes models like, e.g., a relaxed version of the minimal supergravity model [6]. Despite its restrictive boundary conditions, the CMSSM has a rich phenomenology and has been extensively used as a basis for evaluating prospects for SUSY searches at the LHC and in other collider, noncollider, and dark matter (DM) experiments. The model is defined by four continuous parameters and one sign [5]: m_0, the universal scalar mass; $m_{1/2}$, the universal gaugino mass; A_0, the universal trilinear coupling; $\tan\beta$, the ratio of the Higgs vacuum expectation values; and sgnμ, the sign of the Higgs/Higgsino mass parameter μ. We denote them collectively by θ.

So far, the best limits from the LHC experiments ATLAS and CMS have come from channels involving only hadronic final states, with ATLAS investigating jets plus missing transverse momentum, and CMS using jets plus missing transverse energy, a "razor" and α_T [2,7] search methods. In particular, they involve different ways of clustering events into effective dijet systems. Based on 1.1/fb of data the strongest bounds on the scale of SUSY have so far come from the α_T method.

Even before the turn-on of the LHC, the parameter space of the CMSSM had been significantly constrained [8–14] by a variety of experimental data, most notably by LEP

*A.Fowlie@sheffield.ac.uk
†Artur.Kalinowski@fuw.edu.pl
‡Malgorzata.Kazana@fuw.edu.pl
§L.Roszkowski@sheffield.ac.uk
‖Sming.Tsai@fuw.edu.pl
¶On leave of absence from University of Sheffield, Sheffield S3 7RH, United Kingdom.

bounds on electroweak observables, masses of the standard model (SM) and SM-like Higgs boson h and the lighter chargino $\chi_1^\pm$ [3], data on heavy flavor processes $\bar{B} \to X_s \gamma$, $B_u \to \tau\nu$, and $B_s \to \mu^+\mu^-$, the difference between experimental and standard model contributions to the anomalous magnetic moment of the muon $\delta(g-2)_\mu^{\rm SUSY}$ [15], as well as the relic abundance $\Omega_\chi h^2$ [16] of the lightest neutralino, which is assumed to be the dominant component of cold dark matter in the Universe.

In particular, a χ^2 method favored a region of the CMSSM's parameter space with $m_{1/2} \sim$ a few hundred GeV and $m_0 \lesssim m_{1/2}$ [12]. In a Bayesian approach, this region was also favored but in addition a region of parameter space with substantial posterior probability was also found in the so-called horizontal branch, or focus point [17], region of large $m_0 \gtrsim 1$ TeV and $m_{1/2} \ll m_0$ and in, partly overlapping with it, light Higgs resonance region [9,14]. A region of sizable posterior probability also exists in between those two ''islands'' of the highest probability.

While the first results from the LHC had a fairly mild effect on both regions [18–20], the current limits based on the early 2011 data set of ~ 1/fb published so far take a much deeper bite into the $(m_0, m_{1/2})$ plane of the CMSSM [20,21].

Searches for signals of DM in direct detection experiments have over the last few years also led to much improved limits [22]. Most notably, last spring, XENON100 [23,24], with 100.9 days of data, excluded (at 90% C.L.) spin-independent (SI) scattering cross sections $\sigma_p^{\rm SI}$ as low as 10^{-8} pb, for some dark matter particle masses [23]. The impact on the CMSSM's parameter space of this new XENON100 limit has been investigated in combination with 2010 LHC limits in Refs. [20,25,26] and in combination with current LHC limits in Ref. [21]. Moreover, LHCb has recently reported an upper bound on $\mathcal{BR}(B_s \to \mu^+\mu^-)$ [27] that is smaller than the previous best upper bound.

In this paper, our goal is to perform a Bayesian analysis of the CMSSM's parameter space that includes the currently strongest LHC limits on the SUSY mass scale and the XENON100 limit on the DM scattering cross section by carefully estimating associated uncertainties and including them in the likelihood function. Combining limits from different search channels at the LHC is a rather challenging task. In our approach we focus on the result derived by CMS from the α_T method applied to 1.1/fb of data, since it currently provides the strongest constraint on the $(m_0, m_{1/2})$ plane of the CMSSM [20,25,26,28]. We will simulate the α_T experiment at the event level, assume that the experiment was a Poisson process and construct a likelihood map on the CMSSM's $(m_0, m_{1/2})$ plane. Our approach is similar to that of Ref. [19]; however, it differs from that of Refs. [18,21,25], in which the likelihood is modeled with an empirical formula, and from that of Ref. [20], in which the likelihood for the CMS limit is approximated with a step function. In the latter approaches, the likelihood is constructed from the published CMS α_T 95% contour. In contrast, in our approach, the likelihood is constructed in the whole $(m_0, m_{1/2})$ plane and next validated against the official CMS α_T 95% contour.

This paper is organized as follows. In Sec. II we detail our methodology, including our statistical tools, scanning algorithm, and our treatment of the likelihood from the CMS α_T 1.1/fb analysis. In Sec. III we present results of scans that include likelihoods from the CMS α_T 1.1/fb analysis and from XENON100. We summarize our findings in Sec. IV.

II. METHOD

A. The statistical framework

Our goal is to identify the regions of the CMSSM's parameter space that are in best agreement with all relevant experimental constraints, including the α_T and XENON100 limits. The mass spectra and other observables are also dependent on standard model parameters, most notably the top pole mass $m_t^{\rm pole}$, the bottom mass $m_b(m_b)^{\overline{\rm MS}}$, the strong coupling $\alpha_s(M_Z)^{\overline{\rm MS}}$, and $1/\alpha_{\rm em}(M_Z)^{\overline{\rm MS}}$. These ''nuisance'' parameters, which we collectively denote by ϕ, have been shown to play a significant role in a statistical treatment [8–10,14,29].

To set the stage, we define the best-fitting regions with Bayesian and frequentist statistics. In both approaches one considers the likelihood—the probability of obtaining experimental data for observables given the CMSSM's underlying parameters,

$$\mathcal{L}(\theta, \phi) = p(d|\theta, \phi). \tag{1}$$

To see the likelihood's dependence on a particular parameter or set of parameters, one maximizes over the CMSSM's other parameters, to obtain the profile likelihood,

$$\mathcal{L}(\theta) = \max_{\phi} p(d|\theta, \phi). \tag{2}$$

In Bayesian statistics one addresses the question of the posterior—what is the probability of the CMSSM's parameter values given the experimental data? To this end one employs Bayes's theorem to find the posterior probability density function (pdf);

$$p(\theta, \phi|d) = \frac{\mathcal{L}(\theta, \phi)\pi(\theta, \phi)}{p(d)}. \tag{3}$$

The Bayesian approach requires that we articulate our prior knowledge of the CMSSM's parameters in the prior, $\pi(\theta, \phi)$. Finally, the denominator $p(d)$ is the evidence, which, because we are not interested in model comparison, is merely a normalization factor.

To see the posterior's dependence on a particular parameter, or set of parameters, one integrates, or marginalizes, over the CMSSM's other parameters, as well as SM nuisance parameters, to obtain the marginalized posterior pdf.

The two-dimensional region of the CMSSM's, e.g., parameter space $(m_0, m_{1/2})$ that is in best agreement with the experiments, with respect to the posterior—the credible region—is the smallest region, R, that contains a given fraction of the posterior, that is, the smallest region such that

$$\int_R p(m_0, m_{1/2}|d)dm_0\, dm_{1/2} = 1 - \epsilon. \tag{4}$$

The one-dimensional credible region, however, is the region such that the posterior probability of the parameter being above the region is equal to the posterior probability of the parameter being below the region and equal to a given fraction of the posterior. That is, the one-dimensional credible region from L to U of, e.g., m_0, satisfies

$$\int_0^L p(m_0|d)dm_0 = \int_U^\infty p(m_0|d)dm_0 = \frac{1}{2}\epsilon. \tag{5}$$

In the frequentist approach, the k-dimensional region of the CMSSM's parameter space that is in best agreement with the experiments, with respect to the likelihood—the confidence interval—is the region in which the χ^2 is within $\Delta\chi^2$ of the minimum χ^2, where $\Delta\chi^2$ is such that

$$F(\Delta\chi^2, k) = 1 - \epsilon, \tag{6}$$

and $F(\Delta\chi^2, k)$ is a cumulative χ^2 distribution with k degrees of freedom.

The parameter point with the minimum χ^2 (or, equivalently, with the maximum likelihood) is the best-fit point. In frequentist statistics, the best-fit point has a special significance; the confidence intervals are constructed from the best-fit point. In contrast, the best-fit point has no significance in Bayesian statistics.

From the best-fit point, one can obtain a p value: the probability of obtaining a χ^2 value from experimental measurements equal or larger than the best fit χ^2, accounting for the number of degrees of freedom in the fit,

$$p \text{ value} = 1 - F(\chi^2, n), \tag{7}$$

where n, the number of degrees of freedom in the fit, is the number of experimental constraints in the χ^2 calculation minus the number of model parameters that were fitted.

Our credible regions and confidence intervals are defined by Eqs. (4)–(6), with $\epsilon = 0.32$ for 1σ and $\epsilon = 0.05$ for 2σ. In Eq. (6), for a two-dimensional confidence interval, this corresponds to $\Delta\chi^2 = 2.30$ for 1σ and $\Delta\chi^2 = 5.99$ for 2σ.

Scanning the CMSSM's parameter space is computationally intensive—a simple grid scan of an eight-dimensional space is impractical. To scan the CMSSM's parameter space efficiently, we use a modern (2006) Monte Carlo algorithm, called Nested Sampling [30], which is tailored to work with Bayesian statistics. We chose the Nested Sampling settings so that the algorithm would accurately map the posterior, but not necessarily the likelihood, in a reasonable CPU time (4000 live points and a stopping condition of 0.5).

Because of our lack of prior knowledge of the CMSSM's parameters, we invoke the principle of insufficient reason and, as previously in [9,14,31,32] we choose noninformative priors for the CMSSM's parameters that equally weight either linear or logarithmic intervals. The priors that we choose for m_0 and $m_{1/2}$ equally weight logarithmic intervals (log priors). This choice has been shown [14] not to suffer from the volume effect, unlike the flat prior, and it also reduces the amount of fine-tuning needed to achieve radiative electroweak symmetry breaking. For $\tan\beta$, A_0 and for the SM's nuisance parameters we choose equally weighted linear intervals (linear priors). The prior ranges of the CMSSM's parameters and of the SM's nuisance parameters over which we scan are listed in Table I

We use our updated and modified version of the SUPERBAYES [9,14] computer program to perform four scans of the CMSSM:

TABLE I. Priors for the CMSSM's parameters and for the standard model's nuisance parameters that we used in our scans. Masses are in GeV.

Parameter	Description	Prior range	Scale
CMSSM			
m_0	Universal scalar mass	100, 2000	Log
$m_{1/2}$	Universal gaugino mass	100, 1000	Log
A_0	Universal trilinear coupling	−2000, 2000	Linear
$\tan\beta$	Ratio of Higgs VEVs	3, 62	Linear
$\mathrm{sgn}\mu$	Sign of Higgs parameter	+1	Fixed
Nuisance			
m_t^{pole}	Top quark pole mass	163.7, 178.1	Linear
$m_b(m_b)^{\overline{MS}}$	Bottom quark mass	3.92, 4.48	Linear
$\alpha_s(M_Z)^{\overline{MS}}$	Strong coupling	0.1096, 0.1256	Linear
$1/\alpha_{\text{em}}(M_Z)^{\overline{MS}}$	Reciprocal of electromagnetic coupling	127.846, 127.99	Linear

(1) To set the stage for examining the impact of LHC and XENON100 limits, a scan involving constraints from only non-LHC experiments, including those listed above (see Table III for a complete list of observables and their values) but without a likelihood from XENON100.
(2) To validate our method of including the LHC constraints, a scan with a likelihood that we derived from the CMS α_T 1.1/fb, and a likelihood from the experiments that constrain the standard model's nuisance parameters only.
(3) To examine the impact of the current LHC constraints, a scan with a likelihood from non-LHC experiments and from the α_T but without a likelihood from XENON100.
(4) To see the additional impact of the current XENON100 limit scan with a likelihood from non-LHC experiments, the α_T and from XENON100.

B. The efficiency maps for the CMS α_T 1.1/fb analysis

We derived our LHC likelihood for the CMS search [33] for R-parity conserving supersymmetry in all-hadronic events via a kinematic variable α_T. The results based on the LHC data sample of 1.1/fb of integrated luminosity recorded at $\sqrt{s} = 7$ TeV showed no excess of events over the SM predictions. Our aim was to translate the analysis scheme into a simplified approach to obtain the signal selection efficiency for a large number of points in the CMSSM parameter space. To this end we generated a map of points for the CMSSM parameters m_0 in the range of (50, 2000) GeV and $m_{1/2}$ in the range of (50, 1000) GeV, both with a step of 50 GeV. We fixed the values of the other CMSSM parameters: $A_0 = 0$, $\tan\beta = 10$, and $\mathrm{sgn}\mu = 1$. For each point, for a defined set of the CMSSM parameters we calculated a mass spectrum and a table of supersymmetric particle decays using the programs SOFTSUSY [34] and SUSY-HIT [35], respectively. For each point, we then generated 10 000 events with the Monte Carlo generator PYTHIA [36] with a cross-section value obtained at the leading order. We analyzed events at the generator level. Only the geometrical acceptance was applied to simulate the CMS detector response. Leptons were accepted in the pseudorapidity range $\eta < 2.5$ for electrons and $\eta \leq 2.1$ for muons, respectively. The isolation of leptons was checked at the generator level. Stable, generator level particles, excluding neutrinos, were clustered into jets using the anti-k_T algorithm [37], with a cone size parameter $R = 0.5$. Jets were accepted up to $|\eta| < 3$.

The aim of the α_T analysis was to select hadronic events with high transverse momentum jets. Initially, events with at least one jet with transverse momentum $p_T > 50$ GeV and $\eta > 3$ were accepted if no isolated lepton or photon were found in the event, namely, events with an isolated lepton (electron or muon) with $p_T > 10$ GeV or an isolated photon with $p_T > 25$ GeV were rejected. Events had to satisfy a condition based on an H_T variable, defined as $H_T = \sum_{i=1}^{n} E_T^{\mathrm{jet}_i}$; H_T was required to be above 275 GeV. Following the CMS analysis [33], the trigger was fully efficient for selected events, and therefore no attempt to emulate the trigger was made.

The offline analysis used the following H_T binning: 275–325, 325–375, 375–475, 475–575, 575–675, 675–775, 775–875, and >875 GeV. In each H_T bin, we applied the same cuts on transverse momentum of jets (leading, second, others) in the event as in Ref. [33]. Details are shown in Table II.

The main discriminator against QCD multijet production is the variable α_T defined for dijet events as

$$\alpha_T = \frac{E_T^{\mathrm{jet}_2}}{M_T} = \frac{E_T^{\mathrm{jet}_2}}{\sqrt{(\sum_{i=1}^{2} E_T^{\mathrm{jet}_i})^2 - (\sum_{i=1}^{2} p_x^{\mathrm{jet}_i})^2 - (\sum_{i=1}^{2} p_y^{\mathrm{jet}_i})^2}}, \tag{8}$$

where $E_T^{\mathrm{jet}_2}$ is the transverse energy of the less energetic jet in the event with two jets and M_T is a transverse mass of the dijet system defined above.

In events with more than two jets, two pseudojets were formed following the same strategy as in Ref. [33] in such a way that the E_T difference between two pseudojets was minimized. The value of E_T of each of the two pseudojets was obtained by a scalar summing of the contributing E_T^{jet} of jets. In the ideal case, the dijet system had $E_T^{\mathrm{jet}_1} = E_T^{\mathrm{jet}_2}$ and jets are back to back which resulted in a limit of $\alpha_T = 0.5$, where the momentum of jets is large compared to the masses of jets. For back-to-back jets with $E_T^{\mathrm{jet}_1} \neq E_T^{\mathrm{jet}_2}$, values of α_T were smaller than 0.5. Signal events with missing transverse energy resulted in α_T greater than 0.5. Therefore the QCD background was efficiently rejected with

TABLE II. Definition of the H_T bins and the corresponding p_T thresholds for the leading, second, and all other remaining jets in the event. Observed events refers to the number of events passing all α_T cuts for 1.1/fb of data collected by the CMS Collaboration [33].

H_T bin (GeV)	275–325	325–375	375–475	475–575	575–675	675–775	775–875	>875
p_T^{leading} (GeV)	73	87	100	100	100	100	100	100
p_T^{second} (GeV)	73	87	100	100	100	100	100	100
p_T^{others} (GeV)	37	43	50	50	50	50	50	50
				Observed events				
$\alpha_T > 0.55$	782	321	196	62	21	6	3	1

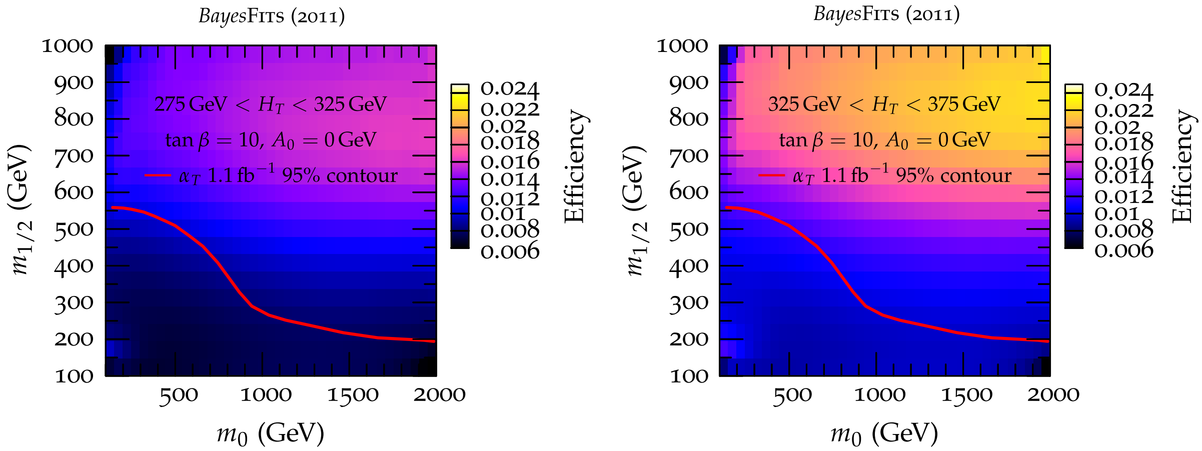

(a) The case of 275 GeV $< H_T <$ 325 GeV.

(b) The case of 325 GeV $< H_T <$ 375 GeV.

FIG. 1 (color online). The efficiency maps of our approximation to the CMS α_T, 1.1/pb on the $(m_0, m_{1/2})$ plane, for tan$\beta = 0$ and $A_0 = 0$, for the two dominant H_T bins.

the final cut of $\alpha_T > 0.55$. The remaining events after all cuts were compared with SM background expectation predictions. No excess was found and the numbers listed in Table II were used as numbers of observed background events.

For the selection defined above, we prepared eight efficiency maps, one for each H_T bin, two of which are shown as examples in Fig. 1.

Experimental selections involving missing transverse energy estimates and selections from an analysis of the distance between a jet and H_T were not implemented, because the relevant variables calculated at the generator level are not reliable. Nevertheless, as discussed below, good agreement between efficiency maps obtained in this analysis, and the CMS result shows that such an approximation is justified.

C. The likelihood from the CMS α_T 1.1/fb analysis

The approximate efficiency maps derived in Sec. II B for the CMS α_T 1.1/fb allow us to evaluate a likelihood, so that we can find the regions of the CMSSM's parameter space in best agreement with the currently strongest LHC limit.

We assume that the experiment can be described by a Poisson distribution; that is, that the events were independent and that the likelihood of observing events was described by a Poisson distribution. We assume that the total number of observed events was the sum of contributions from supersymmetric processes and from SM processes. Following the α_T cuts described in Sec. II B, we consider separately the eight bins of the kinematical variable H_T summarized in Table II.

The number of supersymmetric events that we expected in an ith H_T bin, s_i, is the product of the detector efficiency for that bin (the fraction of events that survive the α_T cuts), ϵ_i, the integrated luminosity, $\int L = 1.1/\text{fb}$, and the total cross section for the production of supersymmetric particles at $\sqrt{s} = 7$ GeV, σ,

$$s_i = \epsilon_i \times \sigma \times \int L. \tag{9}$$

The likelihood for this case, $\mathcal{L}$, which is the probability of observing a set of $\{o_i\}$ events given that we expected $\{s_i\}$ supersymmetric events and $\{b_i\}$ SM background events, is a product of Poisson distribution for each bin with means $\lambda_i = s_i + b_i$,

$$\mathcal{L} = \prod_i \frac{e^{-(s_i+b_i)}(s_i + b_i)^{o_i}}{o_i!}. \tag{10}$$

We assume that standard model backgrounds, b_i, are precisely known. If their experimental errors were significant, the expression for the likelihood would be multiplied by distributions describing the SM backgrounds [38] and they would be included as nuisance parameters. This is not the case for the α_T analysis.

All-hadronic final-state processes are expected to be independent of tanβ and A_0, because these parameters have little influence on the squark and gluino masses, and this has been confirmed by the CMS Collaboration in the CMS α_T 1.1/fb analysis, as well as, e.g., in Refs. [19,39], and also in this study. For this reason we created efficiency maps using the mentioned earlier fixed-grid scan with fixed values of tan$\beta = 10$ and $A_0 = 0$, as described in Sec. II B. The cross section was calculated to leading order with PYTHIA [36].[1] We used this information to produce a likelihood map using Eqs. (9) and (10).

[1]The cross section, and consequently the number of expected supersymmetric events, changes by over 10 orders of magnitude over the $(m_0, m_{1/2})$ plane. The resulting likelihood function is not, therefore, sensitive to next-to-leading order corrections to the cross section. Even if $\sigma_{\text{NLO}} \sim \sigma_{\text{LO}}$, the corrections would only slightly shift the isocontours of the cross section and likelihood on the $(m_0, m_{1/2})$ plane.

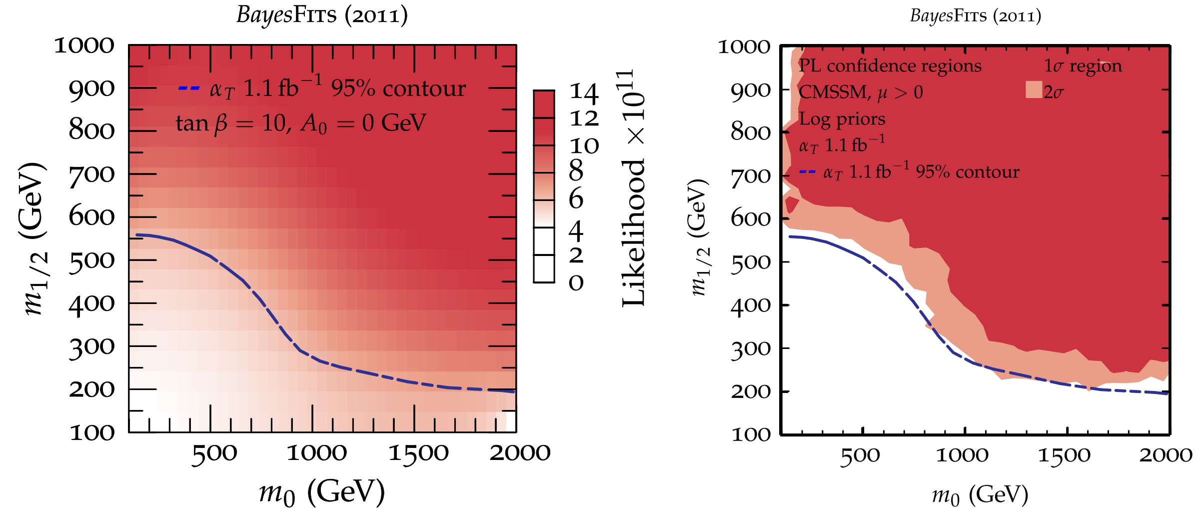

(a) The likelihood map from our CMS α_T 1.1/fb analysis on the $(m_0, m_{1/2})$ plane, for $\tan\beta = 10$ and $A_0 = 0$ using grid scan.

(b) Profile likelihood regions on the $(m_0, m_{1/2})$ plane, with a likelihood from our CMS α_T 1.1/fb analysis, using Nested Sampling and a log prior.

FIG. 2 (color online). The maps of (a) the likelihood and (b) the profile likelihood for our approximation to the CMS α_T, 1.1/pb on the $(m_0, m_{1/2})$ plane. The dashed blue lines show the official CMS 95% exclusion contour.

The resulting likelihood map is shown in Fig. 2(a). It exhibits the correct behavior; below the official 95% contour obtained by CMS α_T 1.1/fb analysis [33], which is also indicated, the likelihood is small. Our approximate 95% contour was calculated with the help of Eq. (6). It corresponds to the boundary of the 2σ range of the profile likelihood obtained using Nested Sampling and a log prior, which is shown in Fig. 2(b), and is very close to the official CMS contour which is also shown in the figure. For each CMSSM point for which our scanning algorithm wished to evaluate the likelihood, we interpolated the likelihood from our likelihood map.

III. RESULTS

In this section we will present our numerical results. To start with, in Table I we show prior ranges and distributions of CMSSM parameters and of SM nuisance parameters, while in Table III we list the observables that we will use in our analysis. These come in three sets. First, by "Non-LHC" we collectively denote all relevant constraints from dark matter, $\Omega_\chi h^2$, precision measurements: $\sin^2\theta_{\rm eff}$, M_W, etc., flavor physics: $\mathcal{BR}(\bar{B} \to X_s\gamma)$, $\mathcal{BR}(B_u \to \tau\nu)$, ΔM_{B_s}, and $\mathcal{BR}(B_s \to \mu^+\mu^-)$, [2] the excess in the anomalous magnetic moment of the muon, $\delta(g-2)_\mu^{\rm SUSY}$, as well as LEP and Tevatron limits on the Higgs sector and superpartner masses. Second, we will apply currently the best limit published by the CMS Collaboration, which is from its α_T analysis of 1.1/fb of data. Finally, at the end we will also apply an upper limit on the elastic scattering of neutralino dark matter $\sigma_p^{\rm SI}$ recently published by XENON100, in order to investigate its additional impact on the CMSSM's parameters and various observables.

Below we will present the results of our scans as one-dimensional (1D) or two-dimensional (2D) marginalized posterior pdf maps of the CMSSM's parameters and observables. In evaluating the posterior pdfs, we marginalized over the CMSSM's other parameters and the SM's nuisance parameters.

A. Impact of the α_T limit

First, in Fig. 3, on the $(m_0, m_{1/2})$ plane, we show the results of a scan with a likelihood from the non-LHC constraints (left panel) and with the additional impact of imposing the α_T 1.1/fb constraint (right panel). Dark (light) blue regions denote the 1σ (2σ) posterior pdf regions of the $(m_0, m_{1/2})$ plane. In Fig. 3(a) one can see two distinct modes on the $(m_0, m_{1/2})$ plane. The vertical 1σ mode is located in the stau coannihilation/A-funnel (SC/AF) region, while the associated 2σ region is caused by the AF only. On the opposite side of the diagonal of the $(m_0, m_{1/2})$ plane, the horizontal mode corresponds to overlapping contributions from the light Higgs resonance region (the narrow 1σ strip) and, above it, the 2σ focus point (FP)/horizontal branch (HB) region.

As a result, the posterior mean (denoted by a solid black dot) lies between the two modes, but closer to the SC/AF region, where the best-fit point (denoted by an encircled cross) is also located. The blue dashed line denoting the

[2] Actually, LHCb [27], an LHC experiment, recently obtained the best upper limit of $\mathcal{BR}(B_s \to \mu^+\mu^-) < 1.5 \times 10^{-8}$, but in this study we will nevertheless include it in the "Non-LHC" group of constraints.

TABLE III. The experimental measurements that constrain the CMSSM's parameters and the standard model's nuisance parameters. Masses are in GeV. The numbers in parentheses in the list of LEP and Tevatron experimental measurements are weaker experimental bounds, which we use for some sparticle mass hierarchies.

Measurement	Mean	Exp. error	The. error	Likelihood distribution	Reference
CMS α_T 1.1/fb analysis					
α_T	See text	See text	0	Poisson	[33]
XENON100					
σ_p^{SI} (m_χ)	$<f(m_\chi)$, see text	0	1000%	Upper limit: error function	[23]
Non-LHC					
$\Omega_\chi h^2$	0.1120	0.0056	10%	Gaussian	[16]
$\sin^2\theta_{\mathrm{eff}}$	0.231 16	0.000 13	0.000 15	Gaussian	[15]
M_W	80.399	0.023	0.015	Gaussian	[15]
$\delta(g-2)_\mu^{\mathrm{SUSY}} \times 10^{10}$	30.5	8.6	1.0	Gaussian	[15]
$\mathcal{BR}(\bar{B} \to X_s \gamma) \times 10^4$	3.60	0.23	0.21	Gaussian	[15]
$\mathcal{BR}(B_u \to \tau\nu) \times 10^4$	1.66	0.66	0.38	Gaussian	[40]
ΔM_{B_s}	17.77	0.12	2.40	Gaussian	[15]
$\mathcal{BR}(B_s \to \mu^+\mu^-)$	$<1.5 \times 10^{-8}$	0	14%	Upper limit: error function	[27]
Nuisance					
$1/\alpha_{\mathrm{em}}(M_Z)^{\overline{\mathrm{MS}}}$	127.916	0.015	0	Gaussian	[15]
m_t^{pole}	172.9	1.1	0	Gaussian	[15]
$m_b(m_b)^{\overline{\mathrm{MS}}}$	4.19	0.12	0	Gaussian	[15]
$\alpha_s(M_Z)^{\overline{\mathrm{MS}}}$	0.1184	0.0006	0	Gaussian	[15]
LEP and Tevatron 95% limits					
m_h	>114.4	0	3	Lower limit: error function	[41]
ζ_h^2	$<f(m_h)$	0	0	Upper limit: step function	[41]
m_χ	>50	0	5%	Lower limit: error function	[42,43]
$m_{\chi_1^\pm}$	>103.5 (92.4)	0	5%	Lower limit: error function	[3,43]
$m_{\tilde{e}_R}$	>100 (73)	0	5%	Lower limit: error function	[3,43]
$m_{\tilde{\mu}_R}$	>95 (73)	0	5%	Lower limit: error function	[3,43]
$m_{\tilde{\tau}_1}$	>87 (73)	0	5%	Lower limit: error function	[3,43]
$m_{\tilde{\nu}}$	>94 (43)	0	5%	Lower limit: error function	[15,44]
$m_{\tilde{t}_1}$	>95 (65)	0	5%	Lower limit: error function	[3,43]
$m_{\tilde{b}_1}$	>95 (59)	0	5%	Lower limit: error function	[3,43]
$m_{\tilde{q}}$	>375	0	5%	Lower limit: error function	[4]
$m_{\tilde{g}}$	>289	0	5%	Lower limit: error function	[4]

95% lower limit derived by the CMS α_T 1.1/fb analysis is marked, but not applied here.

The existence of the two broad regions is consistent with the findings of previous pre-LHC Bayesian analyses [11,14,31], although their relative size does depend on the choice of the prior. Physically they both arise as a result of reducing the relic density of the neutralino, which is generally too large in the part of the $(m_0, m_{1/2})$ plane where χ is the lightest superpartner. In the SC region the density is reduced by a coannihilation with the lighter stau (and other sleptons), and likewise in the AF region it is reduced by neutralino pair annihilation through the pseudoscalar Higgs A funnel, hence the name. Likewise, the same mechanism is at play in the narrow horizontal light Higgs resonance region. In the FP region, on the other hand, as one moves down along a line roughly perpendicular to the diagonal of the $(m_0, m_{1/2})$ plane, the value of μ^2 drops down from large values [for which the lightest supersymmetric particle (LSP) is very binolike, with too large $\Omega_\chi h^2$], and eventually becomes negative, implying a failure of radiative electroweak symmetry breaking conditions. Close to this boundary, in a rather narrow strip of the plane, μ is of order $m_{1/2}$, the LSP develops a sizable Higgsino component, and the relic abundance becomes acceptable.

The impact of the CMS α_T 1.1/fb, which is implemented in our analysis by simulating detector efficiency and evaluating the corresponding likelihood, as described in Sec. II C, is shown in Fig. 3(b). Clearly, the α_T limit has cut deep into the $(m_0, m_{1/2})$ plane's high posterior probability regions—a nominal fraction of the posterior pdf 1σ region is outside of the α_T 95% confidence interval. The α_T limit pushed the credible regions, as well as the best-fit point, to larger values of $m_{1/2}$. Significantly, the two modes on the $(m_0, m_{1/2})$ plane have remained. The 1σ SC/AF region has been pushed up nearly vertically, while the 2σ

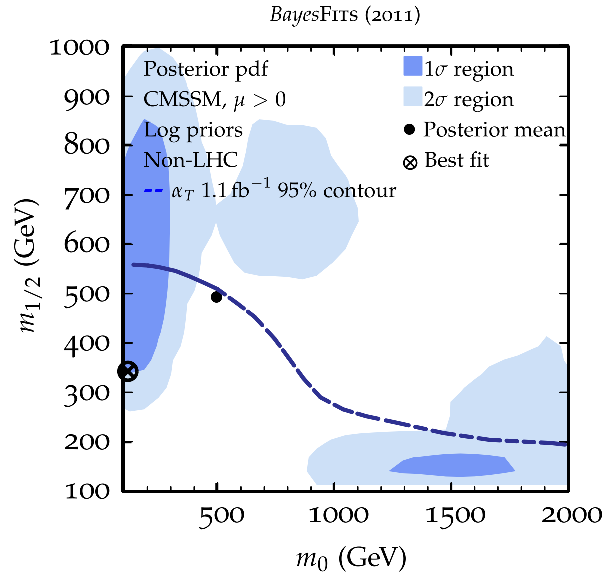

(a) The CMSSM's parameters constrained by the non-LHC experiments only.

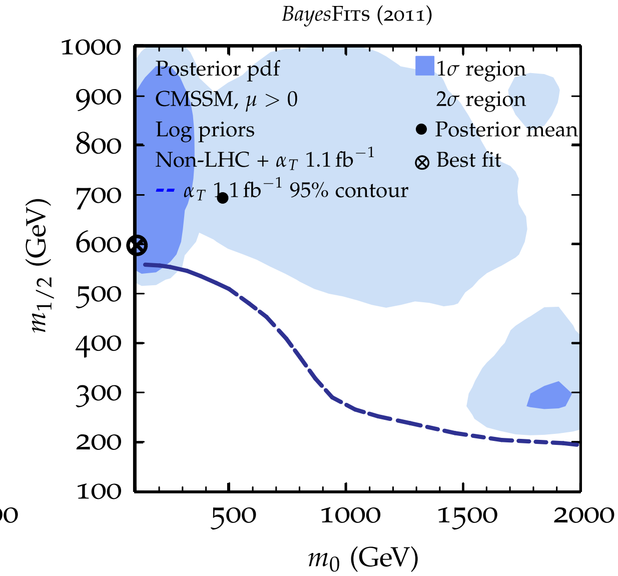

(b) The CMSSM's parameters constrained by the CMS α_T 1.1/fb analysis and by the non-LHC experiments.

FIG. 3 (color online). Marginalized posterior pdf on the $(m_0, m_{1/2})$ plane, (a) before and (b) after we included a likelihood from the CMS α_T 1.1/fb limit.

one of AF only has become inflated and extended to larger values of $(m_0, m_{1/2})$. Note also that the horizontal light Higgs resonance region has now completely disappeared. On the other hand, the FP/HB region is not excluded by the CMS α_T 1.1/fb limit; rather, it is pushed to larger values of m_0 and, to a lesser extent, $m_{1/2}$.

An analogous comparison of the pre- and post-α_T situation in the $(A_0, \tan\beta)$ plane is presented in Figs. 4(a) and 4(b). There are again two 1σ modes: one at relatively small values of $\tan\beta \lesssim 20$ and the other one at much larger values (~ 55), although at 2σ the entire range of scanned values of $\tan\beta$ is allowed. The first mode corresponds to the 1σ stau coannihilation region in Fig. 3(b); however, in the much larger, 2σ, mostly A-funnel region of the $(m_0, m_{1/2})$ plane much larger values of $\tan\beta \sim 55$ are predominant. On the other hand, in the focus point region of large m_0 in Fig. 3(b) we find $25 \lesssim \tan\beta \lesssim 55$.

We can see that the application of the α_T constraint narrows down both modes in the posterior pdf on the $(A_0, \tan\beta)$ plane, primarily as a result of pushing up and out the focus point region, with the effect of strongly disfavoring midrange values of $\tan\beta$. On the other hand the CMS limit shows fairly little effect on A_0, which remains poorly determined.

Although our α_T likelihood is independent of $\tan\beta$ and A_0, it is clear from Fig. 4 that α_T does impact these parameters. The CMSSM's parameters are correlated in a nontrivial way; once the α_T limit is added to the likelihood it alters the best-fitting values of m_0 and $m_{1/2}$ and the values of $\tan\beta$ and A_0 must be adjusted accordingly, so that the predicted values for the CMSSM's observables maintain agreement with the experimental measurements.

In Fig. 5 we show 1D marginalized posterior pdf plots for the CMSSM's parameters, constrained by the non-LHC experiments and by the α_T limit. We also show the dark (light) blue horizontal bars which indicate the one- (two-) dimensional central credible regions. The high probability modes in the m_0 distributions at $m_0 \sim 200$ GeV in Fig. 5(a) and in the $m_{1/2}$ distribution at $m_{1/2} \sim 700$ GeV in Fig. 5(b) correspond to the high probability mode in the SC/AF region in Fig. 3(b). Figure 5(c) shows that the experimental constraints favor positive values of A_0. The two modes in the $\tan\beta$ distribution in Fig. 5(d) correspond to the two modes in Fig. 4.

After marginalization, it is difficult to identify in the m_0 1D marginalized posterior pdf the FP/HB mode, which was present in the 2D marginalized posterior pdf in Fig. 3, though it is present as a second smaller mode in the $m_{1/2}$ 1D marginalized posterior pdf in Fig. 5(b). This is caused by the contribution of the large 2σ credible region at both large $m_{1/2}$ and m_0.

In Fig. 6 we present 1D plots of marginalized posterior pdf for notable particle masses, when we scanned the CMSSM with a likelihood from α_T and from the non-LHC experiments. These distributions are typically bimodal; one mode is from the mode in the SC/AF region and one mode is from the mode in the FP/HB region on the $(m_0, m_{1/2})$ plane in Fig. 3.

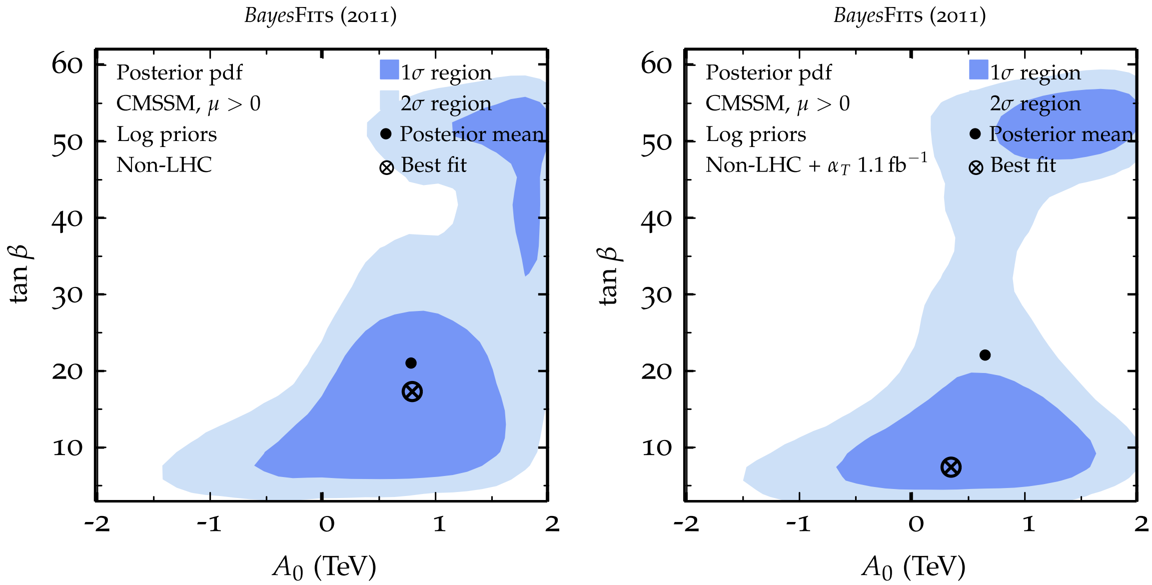

(a) The CMSSM's parameters constrained by the non-LHC experiments.

(b) The CMSSM's parameters constrained by the CMS α_T 1.1/fb analysis and non-LHC experiments.

FIG. 4 (color online). Marginalized posterior pdf on the (A_0, tanβ) plane, (a) before and (b) after we included a likelihood from the CMS α_T 1.1/fb limit.

Figure 6(a) shows that the posterior favors a moderately heavy lightest squark[3] (the lighter stop) with $m_{\tilde{q}} \sim$ 500 GeV, corresponding to the mode in the SC/AF region with small $m_0 \sim 100$ GeV. There is a second, much smaller, mode in the posterior at $m_{\tilde{q}} \sim 1250$ GeV, corresponding to the mode in the FP/HB region with large $m_0 \sim$ 2000 GeV. On the other hand, the squarks of the first two generations can be much heavier, up to ~2.7 TeV at 1σ.

Heavy gluinos, much heavier than lightest squarks, are favored with $m_{\tilde{g}} \lesssim 1500$ GeV, as illustrated in Fig. 6(b). This dominant range corresponds to the mode in the SC/AF region with large $m_{1/2} \sim 700$ GeV. Lighter gluinos with $m_{\tilde{g}} \lesssim 1000$ GeV are not, however, excluded, by the credible region. This is a result of the mode in the FP/HB region.

Figure 6(c) shows that the posterior pdf favors a lightest neutralino mass of $m_\chi \sim 300$ GeV. This corresponds to a binolike neutralino, with $m_\chi \sim 0.4 m_{1/2}$.

Last, Fig. 6(d) shows the 1D posterior pdf for the mass of the lightest Higgs in the CMSSM, in agreement with pre-LHC results [9,10,12,14].

The lightest Higgs boson in the CMSSM is to a very good approximation SM like and the LEP limit (114.4 GeV) applies. Note, however, that predicted Higgs masses below the LEP limit are permitted, because our likelihood function includes a 3 GeV theoretical error in the predicted Higgs mass. On the other side, the 1D posterior pdf is rather narrow, with the 95% credible region in the range from 112.2 to 119.2 GeV and the best-fit value of 114.4 GeV.

Being SM like, the lightest Higgs boson may well be the only Higgs state of the CMSSM accessible in run I. The other Higgses are typically nearly mass degenerate, and much heavier than the lightest Higgs. This is illustrated in Fig. 7, where we present a 2D posterior pdf map on the (A_0, tanβ) plane in two cases: pre-α_T (left panel) and post-α_T (right panel). Figure 7 shows that the α_T limit favors a heavier *CP*-odd neutral Higgs, because it favors higher values of m_0. Intermediate values of tan$\beta \sim 30$, however, are disfavored by α_T, and, consequently, very heavy *CP*-odd neutral Higgs with $m_A \gtrsim 1500$ GeV become disfavored.

B. Impact of the XENON100 limit

The XENON100 Collaboration has recently published a new 90% C.L. exclusion limit on the (m_χ, $\sigma_p^{\rm SI}$) plane which significantly improves their previous preliminary limit [24]. In this section we examine the impact of this new limit on the CMSSM's parameters and observables.

A proper implementation of the XENON100 exclusion limit in our likelihood function is somewhat tricky. The 90% exclusion contour alone is insufficient to reconstruct the likelihood function. On top of it, there are significant errors, which originate from poorly known inputs which are needed in evaluating a limit on $\sigma_p^{\rm SI}$ from experimental data. First, one assumes a "default" value for the local density of value for the local density of 0.3 GeV/c^2, but errors in astrophysical parameters which are required to

[3]The mass of the lightest squark $m_{\tilde{q}} = \min(m_{\tilde{q}i})$.

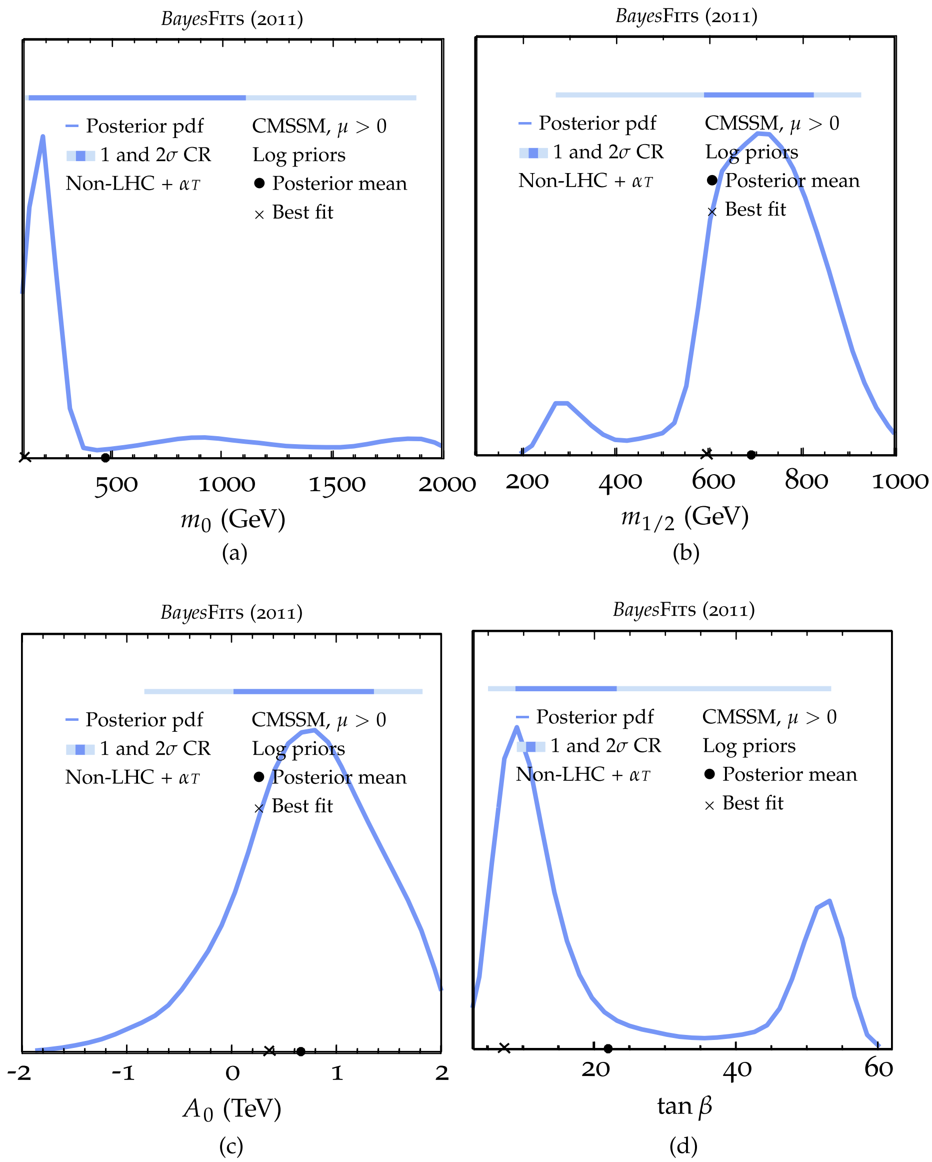

FIG. 5 (color online). One-dimensional marginalized posterior pdf for the CMSSM's parameters constrained by the CMS α_T 1.1/fb analysis and by the non-LHC experiments. The dark (light) blue horizontal bars span the one- (two-)dimensional central credible regions.

determine the local halo and its velocity distribution can result in errors in $\sigma_p^{\rm SI}$ of order 2 [45], although a much better determination has been claimed [46]. More significantly, the fractional error in evaluating $\sigma_p^{\rm SI}$ coming from uncertainties in inputs to hadronic matrix elements can be of order 5, as discussed in detail in [25]. The main uncertainty is due to a poor knowledge of the π-nucleon σ term, $\Sigma_{\pi N}$, which determines the strange quark component of the nucleon.

Given these large uncertainties, we neglect the experimental error in the XENON100 90% exclusion contour and approximate it in the likelihood with a step function, $\mathcal{L}(\sigma_p^{\rm SI}, m_\chi) = 0(1)$ for $\sigma_p^{\rm SI} > (\leq)\sigma_{p,90\%}^{\rm SI}$, where $\sigma_{p,90\%}^{\rm SI}(m_\chi)$ is the DM mass dependent XENON100 90% limit. To incorporate the above errors in evaluating $\sigma_p^{\rm SI}$ in a conservative way, we convolute the step function with a Gaussian with $\mu = \sigma_p^{\rm SI}$ and $\sigma = 10 \times \sigma_p^{\rm SI}$, resulting in a Gaussian error function. This will cause a rather large smearing out of the XENON100 limit.

This can be seen in Fig. 8 where we present the impact of the XENON100 90% C.L. limit (denoted with a solid red curve) on probability maps of the $(m_\chi, \sigma_p^{\rm SI})$ plane for our scans. In Fig. 8(a) the XENON100 limit is not added to the likelihood, while in Fig. 8(b) it is applied. By comparing both panels we can see that, once LHC limits have been applied (left panel), the 1σ posterior region on the $(m_\chi, \sigma_p^{\rm SI})$ plane is only weakly affected by the additional XENON100 limit (right panel).

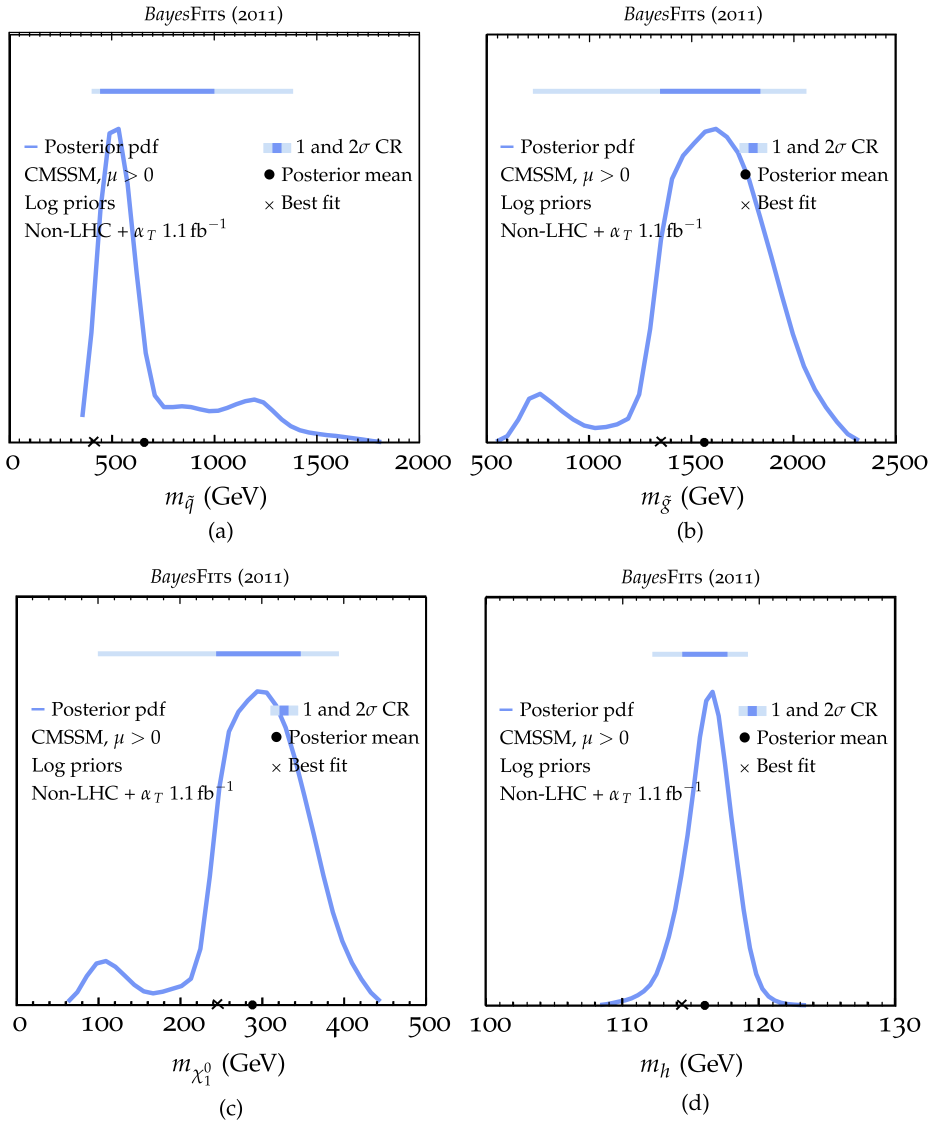

FIG. 6 (color online). The mass of the lightest (a) squark, (b) gluino, (c) neutralino, and (d) Higgs boson in the CMSSM constrained by α_T and by the non-LHC experiments. The horizontal bars have been defined in Fig. 5.

Some interesting effects can nevertheless be noticed. First, a small 2σ region above the XENON100 exclusion curve has shrunk somewhat, especially on the side of larger $\sigma_p^{\rm SI}$, but, because of the large theoretical error assumed in this analysis, it remains allowed. Second, the large smearing affects the favored regions of $\sigma_p^{\rm SI}$ also below the experimental curve. Note that, before the XENON100 is applied [Fig. 8(a)] there are actually two 1σ regions close to each other. The lower one comes entirely from the stau-coannhilation region of small m_0 and large $m_{1/2}$. The other one, just above it (along with a broader 2σ region, both decreasing with m_χ), corresponds to the broad 2σ AF region in the $(m_0, m_{1/2})$ plane. Once the XENON100 limit is added to the likelihood [Fig. 8(b)], the largest values of, just below the experimental curve, become excluded and the statistical significance of the whole AF region becomes reduced to the 2σ level. On the other hand, the lower 1σ region remains nearly intact.

Clearly, recent LHC limits have had the effect of pushing down the most favored ranges of $\sigma_p^{\rm SI}$, for the most part below $\sim 10^{-9}$ pb, while pre-LHC data favored largest 1σ posterior ranges of $\sigma_p^{\rm SI}$ at least an order of magnitude higher; compare, e.g., [14,31]. This implies much poorer prospects for XENON100, with expected reach of $\sim 10^{-9}$ pb to explore the SI cross sections currently favored by the CMSSM.

It is also clear that, in light of the impact of LHC limits, one-ton detectors with planned sensitivity reach of $\sim 10^{-10}$ pb will now be needed to explore the most probable ranges of the $(m_\chi, \sigma_p^{\rm SI})$ plane in the CMSSM. We also note that the most probable range of dark matter particle mass, 250 GeV $\lesssim m_\chi \lesssim$ 343 GeV (at 1σ) is somewhat

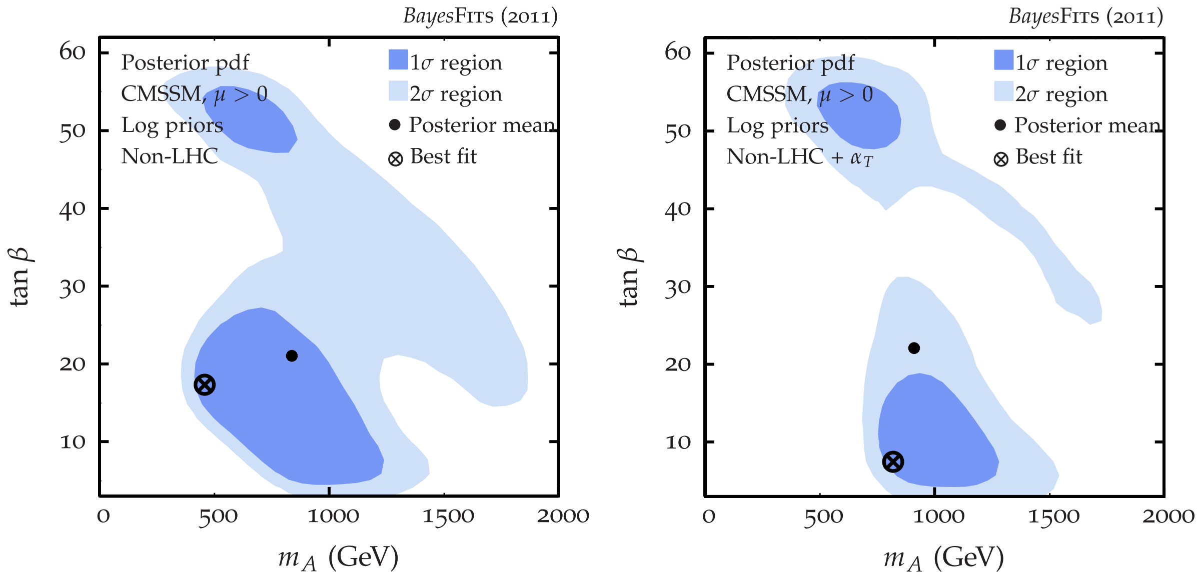

(a) Non-LHC experiments.

(b) CMS α_T 1.1/fb analysis and the non-LHC experiments.

FIG. 7 (color online). Marginalized posterior pdf on the $(m_A, \tan\beta)$ plane, (a) before and (b) after we included a likelihood from the CMS α_T 1.1/fb limit.

above the range of the highest sensitivity of most detectors. Finally, in Table IV, we show the combined impact of the α_T and xenon limits on the posterior ranges of several particle masses already constrained by other (non-LHC) data. The 1σ and 2σ posterior ranges were calculated with Eq. (5).

Finally, in Fig. 9, we show the impact of the XENON100 limit on the shapes of the 2D marginalized posterior pdf maps for the CMSSM parameters. The results shown here correspond to a scan with a likelihood from the non-LHC constraints, from the CMS α_T and 1.1/fb analysis, and from XENON100. The panels should be compared with the corresponding panels in Figs. 3 and 4.

The discussion of Fig. 8 above helps in understanding new effects in Fig. 9. First, it is clear that the configurations of the CMSSM parameters are already constrained by

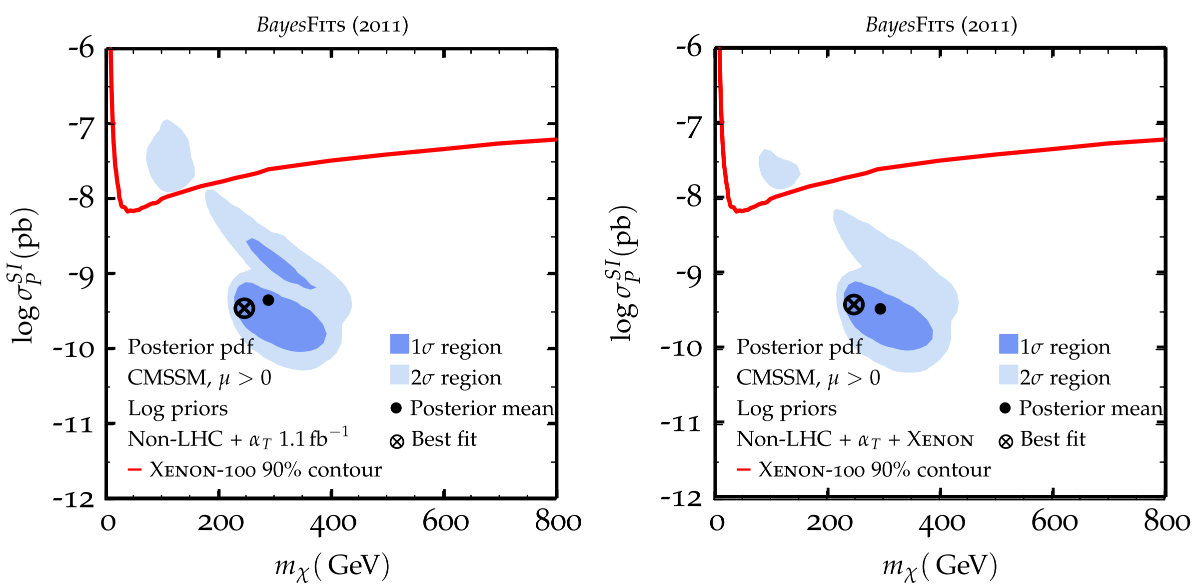

(a) (b)

FIG. 8 (color online). Marginalized posterior pdf on the $(\sigma_p^{\rm SI}, m_\chi)$ plane, (a) before and (b) after we included a likelihood for the XENON100 limit.

TABLE IV. Posterior 1σ and 2σ regions for several particle masses, when constrained by pre- (two left columns) and post-CMS α_T 1.1/fb data, calculated with Eq. (5).

Mass (GeV)	68%	95%	68%	95%
	Non-LHC		Non-LHC + CMS α_T 1.1/fb limit + XENON100	
m_h	(112.3, 116.5)	(110.1, 118.4)	(114.4, 117.8)	(112.2, 119.4)
m_χ	(56, 291)	(53, 356)	(250, 343)	(128, 390)
$m_{\chi_1^\pm}$	(110, 554)	(104, 676)	(475, 651)	(181, 738)
$m_{\tilde{q}}$	(326, 808)	(254, 1172)	(434, 761)	(398, 1302)
$m_{\tilde{g}}$	(403, 1576)	(384, 1885)	(1380, 1825)	(879, 2043)

current LHC limits to give $\sigma_p^{\rm SI}$ for the most part below the XENON100 limit. Unsurprisingly, adding it to the likelihood has a relatively weak additional impact on the CMSSM's parameters. The 1σ posterior region in the high probability SC region on the $(m_0, m_{1/2})$ plane in Fig. 9(a) remains unaffected because the corresponding values of $\sigma_p^{\rm SI}$ are the lowest. The change in the best-fit point is also probably not statistically significant. However, note that the broader 2σ region of AF has shrunk somewhat on the side of large m_0, especially in the direction of the HB/FP region. This is because in that direction the Higgsino component of the DM neutralino increases, causing in turn $\sigma_p^{\rm SI}$ to increase and become at some point constrained by the XENON100 limit, especially for large $\tan\beta$.

Moving farther toward the lower-right corner, we can see that the XENON100 result disfavors also the HB/FP region—the 1σ credible region in the $(m_0, m_{1/2})$ plane in Fig. 3(a) has now become only a 2σ region. This is not surprising since predicted values of $\sigma_p^{\rm SI}$ in that region are among the largest predicted in the CMSSM, again because of the increased Higgsino component of the neutralino. We stress, however, that the HB/FP region is not excluded by the XENON100 limit; rather, it is inside the 2σ credible region. This follows from our conservative estimation of the error in the $\sigma_p^{\rm SI}$ calculation. (We weakened the XENON100 limit by smearing it with a Gaussian describing the theoretical error in the $\sigma_p^{\rm SI}$ calculation.) We have checked that, if we assumed the theoretical error in $\sigma_p^{\rm SI}$ to be $0.1 \times \sigma_p^{\rm SI}$, the limit would exclude the focus point region at 2σ. Finally we note that the favored regions on the $(A_0, \tan\beta)$ plane in Fig. 9(b) are not strongly affected by XENON100, though the two modes on the $(A_0, \tan\beta)$ plane are no longer connected.

C. Prior dependence and the best-fit point

We will now comment on the prior dependence of the results presented here and will also come back to the discussion of the best-fit point.

As is well known, some of the most challenging aspects of Bayesian statistics are the necessity to choose a prior and the sensitivity of the posterior to that choice. The prior dependence of the posterior is a measure of the lack of the constraining power of the likelihood function. If the information from data included in the likelihood is sufficient to

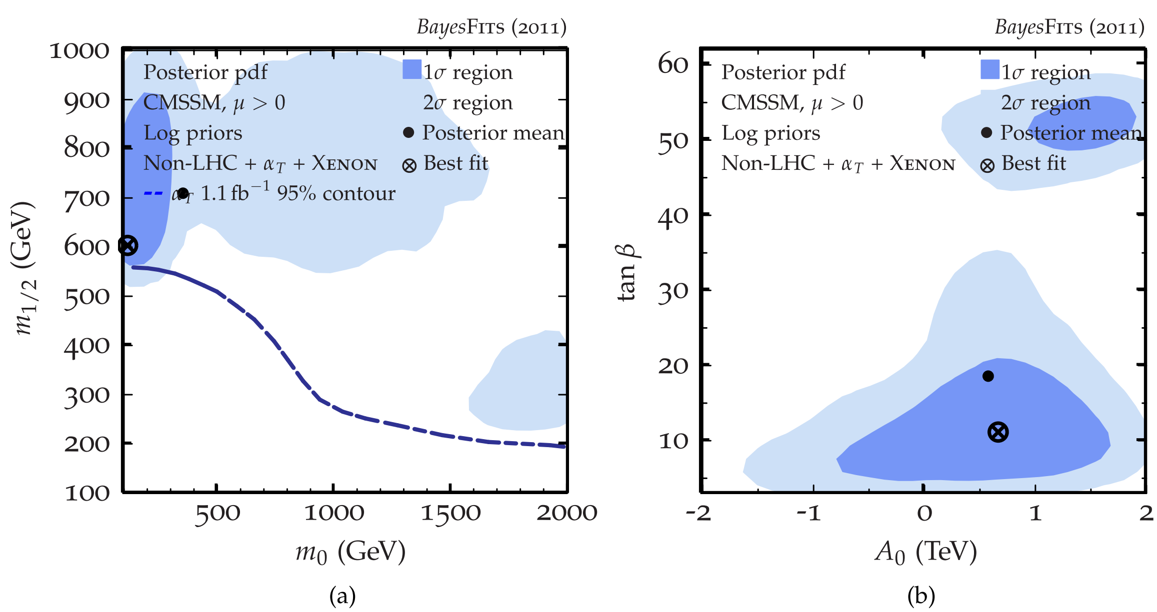

FIG. 9 (color online). Marginalized posterior pdf with the log prior the CMSSM's parameters constrained by non-LHC experiments, the CMS α_T 1.1/fb limit, and the XENON100 limit. The panels should be compared with the corresponding panels in Figs. 3 and 4.

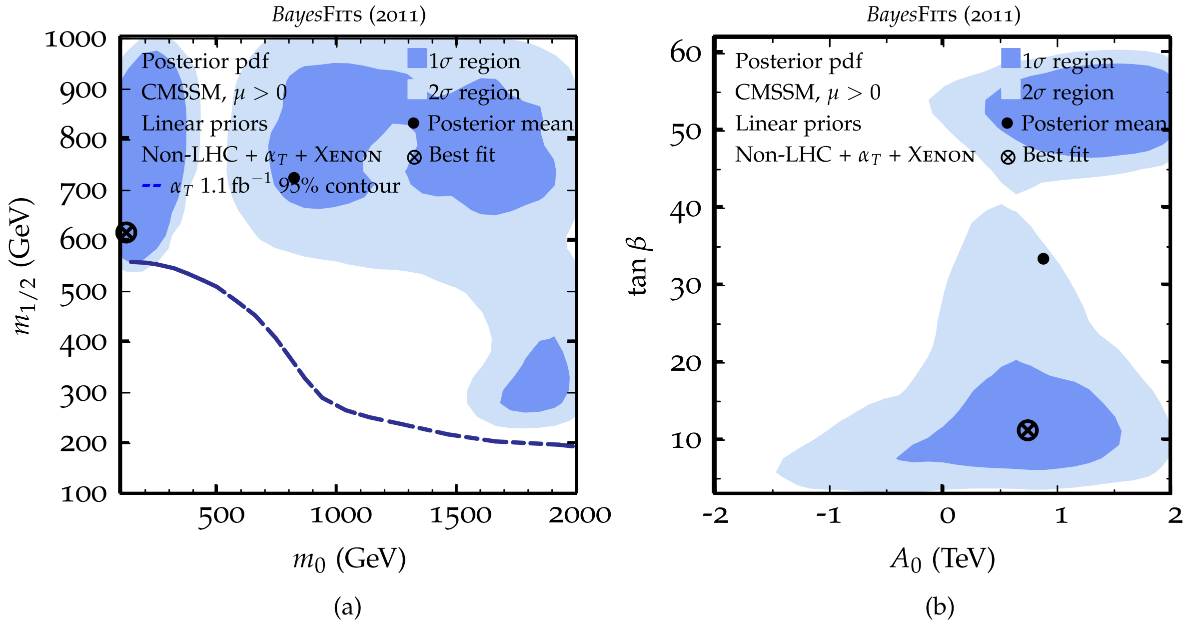

FIG. 10 (color online). Marginalized posterior pdf with the linear (flat) prior the CMSSM's parameters constrained by non-LHC experiments, the CMS α_T 1.1/fb limit, and the XENON100 limit. The figure should be compared with Fig. 9.

select ranges of model's parameters giving good fit to the constraints (high posterior probability regions), then the sensitivity of such ranges to the choice of priors should be weak, or even marginal. In such cases the likelihood has the ability to overpower noninformative priors, such as log priors and linear (flat) priors, and the resulting posterior has little prior dependence. If, however, the posterior is dependent on the choice of prior, the likelihood ought to be regarded as too weak to support robust conclusions about the model.

In several pre-LHC studies prior dependence of the CMSSM was found to be substantial (see, e.g., [14,31]), and the situation in less constrained models was found to be even less satisfactory [47]. This was merely a reflection of poor constraining power of the data available at that time. It was also concluded that the choice of the prior that is linear in the log of the masses is more motivated by both physical and statistical reasons [14,31]. From the physical point of view, log priors explore in much greater detail the low-mass region, where one typically needs less fine-tuning in order to achieve radiative electroweak symmetry breaking. From the statistical point of view, log priors give the same *a priori* weight to all orders of magnitude in the masses, and thus appear to be less biased to giving larger statistical *a priori* weights to the large mass region, which under a flat prior has a much larger volume in parameter space.

Motivated by the above arguments, in this study we have chosen log priors for the CMSSM's mass parameters, and our posterior distributions are, of course, dependent on the choice. As a way of examining the degree of the dependence, we identically repeated our scan of the CMSSM with a likelihood from the non-LHC experiments and from α_T, except that this time we chose linear priors for all the CMSSM's parameters. The resulting posterior distributions, which are shown in Fig. 10, are actually broadly similar to the distributions that resulted from log priors. With linear priors, we found three 1σ modes in the marginalized posterior pdf on the $(m_0, m_{1/2})$ plane, rather than two as in Fig. 3(b). The third mode is present in Fig. 10 both large $m_{1/2}$ and m_0, and probably results from the mentioned above volume effect on the marginalized posterior. For the same reason the 2σ region at large masses also becomes enhanced and the FP/HB mode again becomes strengthened. We interpret this as a reflection of the fact that, despite new strong limits from the LHC, the constraining power of experimental data remains insufficient to eliminate prior dependence of the CMSSM. On the other hand, the effect of assuming the linear prior for $m_{1/2}$ and m_0 on the parameters $\tan\beta$ and m_0 appears to be relatively weaker, as expected, since for the latter the prior has been assumed to be the same (linear) in both cases.

On the other hand, the location of the best-fit point should, by definition, be entirely determined by the likelihood function, and therefore independent of the prior. However, because in practice it is found numerically with a Monte Carlo method, it is a random variable with an error and with a weak dependence on the scanning algorithm, rather than an exact solution. This is clear when one remembers that by choosing, for example, the log prior for the CMSSM's mass parameters, one in practice also chooses a log metric[4] for these parameters. As a result, the

[4]We say metric, rather than prior, to stress that this effect is not related to our choice of Bayesian statistics.

TABLE V. Best-fit points and 68% central credible regions for the CMSSM's parameters, calculated with Eq. (5), when constrained by different sets of experimental data. Masses are in GeV. The best-fit values of m_0 are close to the lower edge of our prior range for m_0, which is 100 GeV; therefore, our central credible regions exclude the best-fit values of m_0.

Constraints	m_0	$m_{1/2}$	A_0	$\tan\beta$	χ^2	d.o.f.	p value
Non-LHC	122 (116, 1391)	343 (142, 702)	806 (236, 1514)	17 (13, 22)	16.53	16	42%
Non-LHC + α_T + XENON100	122 (127, 741)	600 (608, 820)	677 (82, 1283)	11 (9, 16)	22.21	See text	See text

TABLE VI. Breakdown of the main contributions to χ^2 for our best-fit point from a scan with a likelihood from non-LHC experiments and the α_T and XENON100 limits. Note that all likelihoods are normalized to unity, including one for each H_T bin.

Constraint	$\Omega_\chi h^2$	m_h	$\bar{B} \to X_s\gamma$	$\sin^2\theta_{\text{eff}}$	M_W	$\delta(g-2)_\mu^{\text{SUSY}}$	$B_u \to \tau\nu$	ΔM_{B_s}	α_T	Total
χ^2	0.01	1.32	1.98	4.16	1.49	9.76	0.03	0.25	3.42	22.21

scanning algorithm inevitably explores the low-mass region of the CMSSM's $(m_0, m_{1/2})$ plane in greater detail than the high-mass region. This metric dependence can be overcome, or at least reduced, by tightening the algorithm's stopping conditions, so that it runs until it has explored the whole parameter space in sufficient detail. We also emphasize once again that in Bayesian statistics the best-fit point has no significance.

In Table V we present best-fit points from two scans of the CMSSM: one with non-LHC constraints only and one with α_T and XENON100 constraints added to the likelihood. (We quote our best-fit points rounded to the nearest whole GeV or unit of $\tan\beta$.) In both cases the best-fit point is located in the SC/AF region of the CMSSM's parameter space. Our best-fit point for the non-LHC-only case is in good agreement with best-fit points reported previously in Refs. [9–12], which is encouraging. Our p value of 42% is also reasonably close to MasterCode's latest result for the CMSSM of 37% for this case Ref. [21].

On the other hand, after including the α_T and XENON100 constraints in the likelihood, our best-fit point shifts up almost vertically to a larger value of $\simeq 600$ GeV, while the one in Ref. [21] moves much more radically, to much larger values of both mass parameters ($m_0 = 450$ GeV and $m_{1/2} = 780$ GeV), and also giving much larger $\tan\beta = 41$, although with large standard deviations reported for all the parameters.

We investigated which constraints included in the likelihood played the most important role in determining the shape of the posterior, and also the location of the best-fit point. In Table VI we show a breakdown of the main contributions to the χ^2 for the best-fit point corresponding to including the α_T and XENON100 constraints in the likelihood. (Note that the α_T likelihood is itself a product of eight likelihoods, and therefore contributes 8 degrees of freedom, and inevitably has a relatively poor χ^2.) It is clear that the constraint from $\delta(g-2)_\mu^{\text{SUSY}}$ plays the biggest role in increasing the χ^2 for the best-fit point.

The upper panels of Fig. 11 show that the $\delta(g-2)_\mu^{\text{SUSY}}$ constraint requires that increases in $m_{1/2}$ induced by the α_T limit are compensated by increases in m_0 [Fig. 11(a)], and also in $\tan\beta$ [Fig. 11(b)]. Our best-fit point is, however, being pulled in a different direction mostly by $\mathcal{BR}(\bar{B} \to X_s\gamma)$. The lower panels of Fig. 11 show that increasing $m_{1/2}$ by improving LHC mass limits does not require one to increase m_0 [Fig. 11(c)] and small $\tan\beta$ is sufficient [Fig. 11(d)], in order to maintain a good fit to $\mathcal{BR}(\bar{B} \to X_s\gamma)$. There is a clear tension between, on the one hand, $\delta(g-2)_\mu^{\text{SUSY}}$, which favors lighter mass spectra in order to generate large enough SUSY contribution to the variable, and, on the other hand, $\mathcal{BR}(\bar{B} \to X_s\gamma)$ and other constraints which prefer a SUSY contribution to be all but suppressed.[5] The tension between the two observables is exacerbated by adding the constraint from α_T, because it pushes $m_{1/2}$ into a region of the $(m_0, m_{1/2})$ plane in which it is more difficult to satisfy both constraints simultaneously. It appears that, at the end $\delta(g-2)_\mu^{\text{SUSY}}$ is outweighed by the other constraints, most notably $\mathcal{BR}(\bar{B} \to X_s\gamma)$. As a result, we find that the best-fit point remains at small m_0 and $\tan\beta$, and $\delta(g-2)_\mu^{\text{SUSY}}$ is forsaken. Consequently, the best-fit points have a large χ^2 from $\delta(g-2)_\mu^{\text{SUSY}}$ but not from $\mathcal{BR}(\bar{B} \to X_s\gamma)$; compare Table VI.

To investigate its effect, we repeated our analysis without the $\delta(g-2)_\mu^{\text{SUSY}}$ experimental constraint. With a likelihood from non-LHC experiments, except for $\delta(g-2)_\mu^{\text{SUSY}}$, and from α_T, the credible regions on the $(m_0, m_{1/2})$ plane are similar to those in Fig. 3(b), though the central region of the plane is disfavored. The best-fit point's value of $m_{1/2}$ is significantly larger than that in Fig. 3(b). This suggests that, while it favors smaller values of the SUSY mass parameters, $\delta(g-2)_\mu^{\text{SUSY}}$ does not play the dominant role in determining the credible regions.

This is further illustrated in Fig. 12(a), where we show the interplay between combinations of constraints from $\mathcal{BR}(\bar{B} \to X_s\gamma)$, $\mathcal{BR}(B_s \to \mu^+\mu^-)$, $\delta(g-2)_\mu^{\text{SUSY}}$, and $\Omega_\chi h^2$ in 2D marginalized posteriors. We can also see

[5]The tension between $\delta(g-2)_\mu^{\text{SUSY}}$ and $\mathcal{BR}(\bar{B} \to X_s\gamma)$ has already been investigated in Ref. [31] for the pre-LHC case.

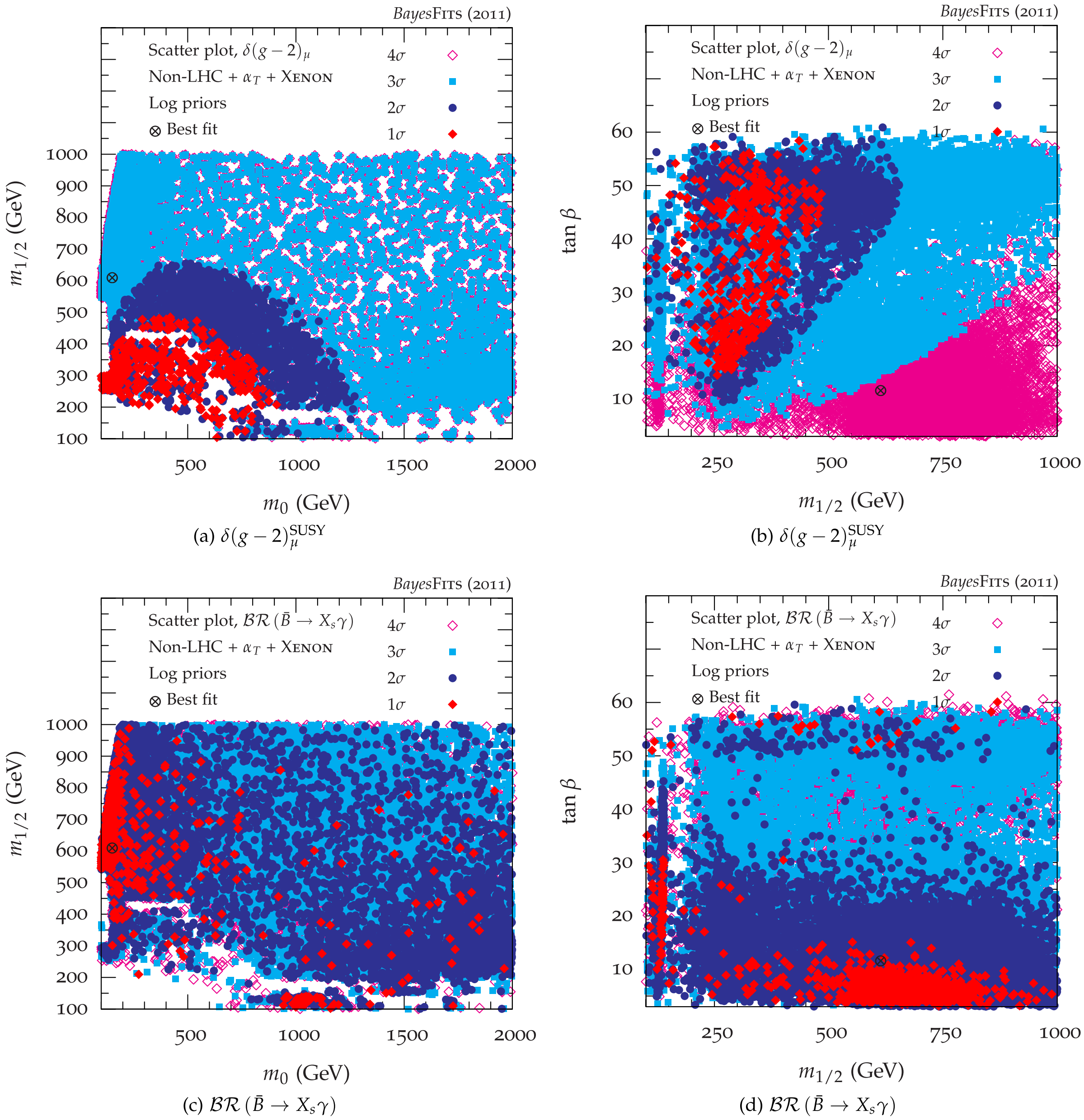

FIG. 11 (color online). Scatter plots of points from a scan with a likelihood from the α_T and XENON100 limits and from non-LHC experiments, colored by the values of $\delta(g-2)_\mu^{\rm SUSY}$ (top row) and $\mathcal{BR}(\bar{B}\to X_s\gamma)$ (bottom row). The colors show the discrepancy between the CMSSM's predicted value and the central experimental value, measured in experimental errors.

that the resulting range of $\mathcal{BR}(B_s\to\mu^+\mu^-)$ is very close to its SM value and that $\Omega_\chi h^2$ plays a rather neutral role in determining both the posterior and the best-fit point. This is because one can relatively easily adjust A_0 to produce the correct value of $\Omega_\chi h^2$, without much affecting the other major constraints.

Another note is in order about χ^2 and the p value. As can be seen from Table V, applying only non-LHC constraints, we find $\chi^2 = 16.53$ and the p value of 42%. Adding new constraints from the α_T and XENON100 likelihood inevitably increases the value of χ^2, but a shift in the p value depends on our assumptions about the additional degrees of freedom. In the CMS analysis [33] the observed events in each bin are treated as independent of the other bins and described by a Poisson distribution. This is why in our treatment of the α_T limit we evaluated likelihood in each of the eight energy bins independently, treating them as contributing as many new degrees of freedom. In this case the p value in fact increases to 61%. On the other hand, one could reasonably expect that signal events in different bins would be correlated, in which case the α_T constraint could be treated as effectively contributing only one extra degree of freedom. In this case the resulting p value would be 22.3%. This illustrates the difficulty in correctly estimating

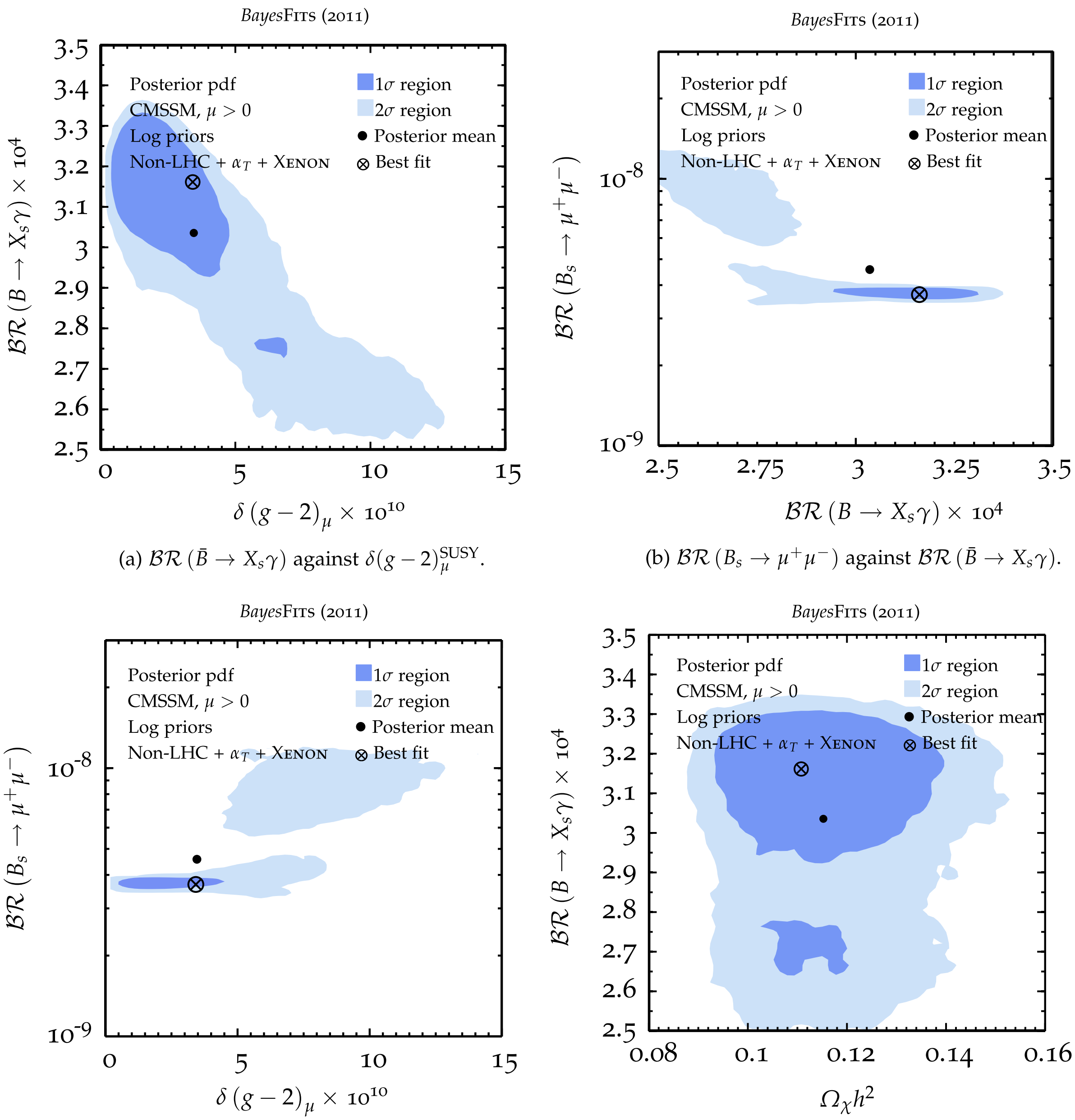

(a) $\mathcal{BR}\,(\bar{B} \to X_s\gamma)$ against $\delta(g-2)_\mu^{\mathrm{SUSY}}$.

(b) $\mathcal{BR}\,(B_s \to \mu^+\mu^-)$ against $\mathcal{BR}\,(\bar{B} \to X_s\gamma)$.

(c) $\mathcal{BR}\,(B_s \to \mu^+\mu^-)$ against $\delta(g-2)_\mu^{\mathrm{SUSY}}$.

(d) $\mathcal{BR}\,(\bar{B} \to X_s\gamma)$ against Ωh^2.

FIG. 12 (color online). Marginalized posterior pdf for combinations of the experimental observables $\mathcal{BR}(\bar{B} \to X_s\gamma)$, $\delta(g-2)_\mu^{\mathrm{SUSY}}$, $B_s \to \mu^+\mu^-$, and Ωh^2, from a scan with a likelihood from α_T, XENON100, and non-LHC experiments.

the number of degrees of freedom and the p value. We also note that in a recent analysis of the MasterCode [21] the p value diminished from 37% to 15% when the LHC and XENON100 constraints were included. Note, however, that in that analysis Gaussian distributions were assumed, unlike here. Also, their way of including LHC limits from jets + $\not{E}_T$ in the likelihood contributed only 1 additional degree of freedom and also forward-backward scattering variables A_{fb} were included in their likelihood, which suppressed their p values further. All this makes it difficult to compare the resulting values of χ^2 and p value.

In addition to a different location of the best-fit point and the p value, the confidence intervals on the $(m_0, m_{1/2})$ plane that are found in Ref. [21] are much larger than our confidence intervals and span the central region. On the other hand, they do not include the focus point region. In contrast, we find regions of the largest posterior not only in the SC/AF region but also in the focus point region, both in the pre-LHC case, in agreement with previous studies using the SUPERBAYES code [14], and also after including the α_T and XENON100 limits. A physical reason for its existence has been given earlier.

The apparent discrepancy between some of the results reported here and those in a recent χ^2 analysis by the MasterCode group [25] is probably caused by a combination of several factors. Some have already been mentioned above. Most likely, the different ways of implementing LHC limits play an important role.[6] We also note that the implementation of $\mathcal{BR}(\bar{B} \to X_s \gamma)$ in the version of SUPERBAYES that we have used for this analysis differs from that of the MasterCode group whose experimental constraint is the ratio of the measured branching ratio to its standard model prediction. In contrast, in SUPERBAYES the constraint from $\mathcal{BR}(\bar{B} \to X_s \gamma)$ is simply applied to the measured branching ratio. On the other hand, the choice of different statistics (Bayesian vs χ^2) is probably of secondary importance since our results for the best-fit point agree reasonably well in the non-LHC case with several other analyses, both Bayesian and χ^2, [14,18,19,28]. We also note that the large 1σ errors reported on the CMSSM parameters for the best-fit point in [25] indicate to us that probably small differences in the likelihood function may lead to large shifts in the location of the best-fit point, in addition to numerical issues related to using different scanning algorithms. This may imply that the high probability regions of the CMSSM parameter space after including current LHC constraints are quite "unstable," or can fairly easily shift within a rather wide plateau, in the sense that "secondary" issues such as the precise implementation of some of the main constraints, or a treatment of LHC limits may lead to major differences, and seemingly contradictory results.

IV. SUMMARY

We have performed an updated Bayesian analysis of the CMSSM. In addition to updating experimental inputs in indirect modes of constraining SUSY [most notably $\mathcal{BR}(B_s \to \mu^+\mu^-)$], we included much improved limits from the α_T 1.1/fb, which currently gives the strongest bounds on the CMSSM mass parameters, and from the XENON100 experiment. We simulated the α_T in an approximate but methodologically correct way by estimating the efficiency for the α_T method and constructing a likelihood function. We validated our method against the official CMS 95% contour. For the XENON100 limit we constructed a conservative, approximate likelihood function by taking into account large uncertainties related to the inputs to hadronic matrix elements and the local density of dark matter.

We incorporated these likelihoods into a global Bayesian fit of the CMSSM and identified marginalized posterior maps of the CMSSM's parameter space. These credible regions were compared with credible regions before the new experiments to illustrate the effects of the new constraints. The α_T limit has taken a deep bite into regions of the CMSSM's parameter space that were previously favored, and has pushed the best-fit point to significantly higher values of $m_{1/2}$. Including XENON100 in the likelihood had a weak additional effect. We find that, although the focus point region is disfavored by the new constraints, it is still not excluded.

Despite the disappointing null results of SUSY searches at the LHC so far, which have pushed the allowed ranges of CMSSM mass parameters, especially $m_{1/2}$, up to much larger values, we note that the best-fit point, both before and after including the CMS α_T, 1.1/pb, is found close to the bottom of the marginalized 1σ posterior ranges of both m_0 and $m_{1/2}$. Despite the uncertainties in determining its location discussed above, this is certainly encouraging for prospects of finding a signal of SUSY in a much larger data set already collected by both ATLAS and CMS. On the other hand, we note that the preference for the low-mass spectrum in the CMSSM and similar unified models is driven primarily by a $\delta(g-2)_\mu^{\mathrm{SUSY}}$ anomaly, satisfying what has already been in some tension with $\mathcal{BR}(\bar{B} \to X_s \gamma)$, and is now becoming increasingly harder also with improving LHC limits.

[6] L. R. and J. Ellis (private communication).

ACKNOWLEDGMENTS

A. J. F. is funded by the Science Technology and Facilities Council. L. R. and S. T. are funded in part by the Welcome Programme of the Foundation for Polish Science. L. R. is also supported in part by the Polish National Science Centre Grant No. N N202 167440, an STFC consortium grant of Lancaster, Manchester, and Sheffield Universities, and by the EC 6th Framework Program No. MRTN-CT-2006-035505.

[1] G. Aad *et al.* (ATLAS Collaboration), arXiv:1109.6572.

[2] S. Chatrchyan *et al.* (CMS Collaboration), Phys. Rev. Lett. **107**, 221804 (2011).

[3] LEP SUSY Working Group for the ALEPH, DELPHI, L3, and OPAL Collaborations, http://lepsusy.web.cern.ch/lepsusy.

[4] V. Abazov *et al.* (D0 Collaboration), Phys. Lett. B **680**, 34 (2009); T. Aaltonen *et al.* (CDF Collaboration), Phys. Rev. Lett. **101**, 251801 (2008); Phys. Rev. D **82**, 092001 (2010).

[5] G. L. Kane, C. F. Kolda, L. Roszkowski, and J. D. Wells, Phys. Rev. D **49**, 6173 (1994); S. P. Martin, arXiv:hep-ph/9709356.

[6] A. H. Chamseddine, R. L. Arnowitt, and P. Nath, Phys. Rev. Lett. **49**, 970 (1982); P. Nath, R. L. Arnowitt, and A. H. Chamseddine, Nucl. Phys. **B227**, 121 (1983); L. J. Hall, J. D. Lykken, and S. Weinberg, Phys. Rev. D **27**, 2359 (1983).
[7] G. Lungu *et al.* (CMS Collaboration), arXiv:0910.3310.
[8] B. Allanach and C. Lester, Phys. Rev. D **73**, 015013 (2006); B. Allanach, Phys. Lett. B **635**, 123 (2006).
[9] R. R. de Austri, R. Trotta, and L. Roszkowski, J. High Energy Phys. 05 (2006) 002.
[10] B. C. Allanach, K. Cranmer, C. G. Lester, and A. M. Weber, J. High Energy Phys. 08 (2007) 023.
[11] F. Feroz, B. C. Allanach, M. Hobson, S. S. AbdusSalam, R. Trotta, and A. M. Weber, J. High Energy Phys. 10 (2008) 064.
[12] O. Buchmueller *et al.*, Eur. Phys. J. C **71**, 1583 (2011).
[13] R. Trotta, R. R. de Austri, and L. Roszkowski, New Astron. Rev. **51**, 316 (2007); B. C. Allanach, C. G. Lester, and A. M. Weber, J. High Energy Phys. 12 (2006) 065; O. Buchmueller, R. Cavanaugh, A. De Roeck, S. Heinemeyer, G. Isidori, P. Paradisi, F. J. Ronga, A. M. Weber, and G. Weiglein, Phys. Lett. B **657**, 87 (2007); J. High Energy Phys. 09 (2008) 117.
[14] R. Trotta, F. Feroz, M. P. Hobson, L. Roszkowski, and R. Ruiz de Austri, J. High Energy Phys. 12 (2008) 024; F. Feroz, M. P. Hobson, L. Roszkowski, R. Ruiz de Austri, and R. Trotta, arXiv:0903.2487; L. Roszkowski, R. Ruiz de Austri, and R. Trotta, Phys. Rev. D **82**, 055003 (2010); O. Buchmueller *et al.*, Eur. Phys. J. C **64**, 391 (2009).
[15] K. Nakamura *et al.* (Particle Data Group), J. Phys. G **37**, 075021 (2010); J. P. Miller, E. de Rafael, and B. L. Roberts, Rep. Prog. Phys. **70**, 795 (2007).
[16] E. Komatsu *et al.* (WMAP Collaboration), Astrophys. J. Suppl. Ser. **192**, 18 (2011).
[17] K. L. Chan, U. Chattopadhyay, and P. Nath, Phys. Rev. D **58**, 096004 (1998); J. L. Feng, K. T. Matchev, and T. Moroi, Phys. Rev. D **61**, 075005 (2000).
[18] O. Buchmueller *et al.*, Eur. Phys. J. C **71**, 1634 (2011); B. C. Allanach, T. J. Khoo, C. G. Lester, and S. L. Williams, J. High Energy Phys. 06 (2011) 035.
[19] B. C. Allanach, Phys. Rev. D **83**, 095019 (2011).
[20] G. Bertone, D. G. Cerdeñob, M. Fornasa, R. Ruiz de Austri, C. Strege, and R. Trotta, J. Cosmol. Astropart. Phys. 01 (2012) 015.
[21] O. Buchmueller, R. Cavanaugh, A. De Roeck, M. J. Dolan, J. R. Ellis, H. Flacher, S. Heinemeyer, G. Isidori, D. Martinez Santos, K. A. Olive, S. Rogerson, F. J. Ronga, and G. Weiglein, arXiv:1110.3568; M. Farina, M. Kadastik, D. Pappadopulo, J. Pata, M. Raidal, and A. Strumia, Nucl. Phys. **B853**, 607 (2011); S. Profumo, Phys. Rev. D **84**, 015008 (2011).
[22] J. Angle *et al.* (XENON10 Collaboration) Phys. Rev. D **80**, 115005 (2009); Z. Ahmed *et al.* (CDMS-II Collaboration), Science **327**, 1619 (2010).
[23] E. Aprile *et al.* (XENON100 Collaboration), Astropart. Phys. **35**, 573 (2012).
[24] E. Aprile *et al.* (XENON100 Collaboration), Phys. Rev. Lett. **107**, 131302 (2011).
[25] O. Buchmueller *et al.*, Eur. Phys. J. C **71**, 1722 (2011).
[26] S. Akula, D. Feldman, Z. Liu, P. Nath, and G. Peim, Mod. Phys. Lett. A **26**, 1521 (2011).
[27] R. Aaij *et al.* (LHCb Collaboration), Phys. Lett. B **699**, 330 (2011).
[28] P. Bechtle *et al.*, arXiv:1105.5398.
[29] B. Allanach, G. A. Blair, A. Freitas, S. Kraml, H.-U. Martyn, G. Polesello, W. Porod, and P. M. Zerwas, Nucl. Phys. B, Proc. Suppl. **135**, 107 (2004).
[30] F. Feroz, M. P. Hobson, and M. Bridges, Mon. Not. R. Astron. Soc. **398**, 1601 (2009).
[31] L. Roszkowski, R. R. de Austri, and R. Trotta, J. High Energy Phys. 04 (2007) 084; L. Roszkowski, R. Ruiz de Austri, and R. Trotta, J. High Energy Phys. 07 (2007) 075.
[32] D. E. Lopez-Fogliani, L. Roszkowski, R. R. de Austri, and T. A. Varley, Phys. Rev. D **80**, 095013 (2009).
[33] CMS Collaboration, Report No. CMS-PAS-SUS-11-003, 2011.
[34] B. C. Allanach, Comput. Phys. Commun. **143**, 305 (2002).
[35] A. Djouadi, M. M. Muhlleitner, and M. Spira, Acta Phys. Pol. B **38**, 635 (2007).
[36] T. Sjostrand, P. Edén, C. Friberg, L. Lönnblad, G. Miu, S. Mrenna, and E. Norrbin, Comput. Phys. Commun. **135**, 238 (2001).
[37] M. Cacciari, G. P. Salam, and G. Soyez, J. High Energy Phys. 04 (2008) 063.
[38] F. Loparco and M. Mazziotta, Nucl. Instrum. Methods Phys. Res., Sect. A **646**, 167 (2011).
[39] P. Bechtle, B. Sarrazin, K. Desch, H. K. Dreiner, P. Wienemann, M. Krämer, C. Robens, and B. O'Leary, Phys. Rev. D **84**, 011701 (2011).
[40] D. Asner *et al.* (Heavy Flavor Averaging Group), arXiv:1010.1589.
[41] R. Barate *et al.* (LEP Working Group for Higgs boson searches, ALEPH Collaboration, DELPHI Collaboration, L3 Collaboration, and OPAL Collaboration), Phys. Lett. B **565**, 61 (2003).
[42] A. Heister *et al.* (ALEPH Collaboration), Phys. Lett. B **583**, 247 (2004).
[43] A. Heister *et al.* (ALEPH Collaboration), Phys. Lett. B **526**, 206 (2002); P. Achard *et al.* (L3 Collaboration), Phys. Lett. B **580**, 37 (2004).
[44] J. Abdallah *et al.* (DELPHI Collaboration), Eur. Phys. J. C **31**, 421 (2003).
[45] M. Pato, L. Baudis, G. Bertone, R. Ruiz de Austri, L. E. Strigari, and R. Trotta, Phys. Rev. D **83**, 083505 (2011).
[46] R. Catena and P. Ullio, J. Cosmol. Astropart. Phys. 08 (2010) 004.
[47] L. Roszkowski, R. Ruiz de Austri, R. Trotta, Y.-L. S. Tsai, and T. A. Varley, Phys. Rev. D **83**, 015014 (2011).